Materials Today • Volume xxx, Number xx • xxxx 2024

ELSEVIER

All-cellulose hydrogel with ultrahigh stretchability exceeding 40000%

Yifan Zhang [a,1], Xia Sun [a,1], Yuhang Ye [a], Hale Oguzlu [a], Yeling Zhu [a], Jiaying Zhu [a], Katherine Le [b], Pu Yang [a], Feng Jiang [a,*]

[a] Sustainable Functional Biomaterials Laboratory, Department of Wood Science, The University of British Columbia, Vancouver, British Columbia V6T 1Z4, Canada
[b] Flexible Electronics and Energy Lab, Department of Electrical and Computer Engineering, University of British Columbia, Vancouver, BC V6T 1Z4, Canada

While cellulose-based stretchable hydrogels have been extensively explored in recent years, all-cellulose hydrogels continue to face the limitation of low stretchability (less than 250 %). Herein, for the first time, we fabricate an all-cellulose hydrogel with ultrahigh stretchability that can exceed 40000 % strain. By ring opening reaction on cellulose anhydroglucose unit rings, secondary hydroxyls are converted to primary hydroxyls, enabling enhanced chain flexibility, and facilitating the formation of abundant hydrogen bonds. As a result, the obtained hydrogel displays remarkable characteristics, including record-high stretchability (44200 %), rapid self-healing property (within seconds), and the unique ability to form cellulose fiber. With simple drawing, a smooth and flexible cellulose fiber can be obtained, demonstrating good processability and a high tensile strength of 226 MPa. Furthermore, the all-cellulose hydrogel can function as a human motion sensor and electrocardiogram electrode for monitoring physiological signals. This simple yet highly effective method will not only propel the advancement of ultrastretchable all-cellulose hydrogels but also create new possibilities for wearable device applications.

Keywords: All-cellulose hydrogel; Ultra-stretchable; Self-healing; Dialcohol cellulose; Hydrogen bonding

Introduction

Hydrogel, an emerging material composed of a polymeric network that encapsulates a significant amount of water, has gained significant attention in diverse fields, including biomedical engineering [1–3], flexible electronics [4–6], and energy storage and conversion [7–9]. To guarantee optimal performance in real-world application scenarios, the selection of an exceptional polymeric backbone is paramount, as it significantly influences overall performance outcomes. Synthetic polymers such as polyacrylic acid (PAA), polyacrylamide (PAAm), and polyvinyl alcohol (PVA) currently dominate both the research and commercial sectors in hydrogel fabrication, owing to their exceptional mechanical properties, significant water absorption capacity, and easy processibility [10–15]. However, these synthetic polymers, derived from petrochemicals, are not biodegradable, posing serious environmental concerns [16–18]. Consequently, discovering an environmentally friendly alternative for high-performance hydrogel preparation holds significant importance.

In nature, hydrogel-like structures are abundant in multicellular organisms [19–24]. For instance, vascular and nonvascular (e.g., algae) plants can be considered as hydrogels during specific stages of their growth [20]. In these cases, cellulose acts as the fundamental building block, forming a 3D interconnected

* Corresponding author.
E-mail address: Jiang, F. (feng.jiang@ubc.ca)
[1] Yifan Zhang and Xia Sun contributed equally to this work.

Please cite this article in press as: Y. Zhang et al., Materials Today (2024), https://doi.org/10.1016/j.mattod.2024.02.007

network that swells in water while maintaining structural integrity, thanks to its strong hygroscopicity and extraordinary mechanical strength derived from inter- and intra-molecular hydrogen bonds [20]. Due to its biodegradability, abundant availability, and a host of other beneficial properties, cellulose has gained widespread recognition as the most promising environmentally friendly candidate for the fabrication of hydrogels and other advanced devices [25–34]. Nevertheless, native cellulose hydrogels exhibit inherent stiffness, primarily attributed to the presence of rigid anhydroglucose unit (AGU) and the highly ordered, crystalline structures formed by extensive intra- and inter-chain hydrogen bonding. Although stretchable cellulose-based hydrogels have been reported, cellulose typically constitutes a minimal fraction within the hydrogel system, primarily functioning as reinforcement filler by harnessing its rigid and high modulus properties. The stretchability of these hydrogels primarily arises from the synthetic polymer network [28,35–40].

Breaking and reconstructing intermolecular hydrogen bonds by dissolving cellulose into molecular chains and regenerating them in an anti-solvent bath has been proposed as a solution to this limitation [41–44]. The transformation from Cellulose I to Cellulose II allomorph has shown the potential to enhance the elasticity and stretchability of the resulting hydrogel [45]. Furthermore, the presence of water molecules as a plasticizer contributes to the further increase in stretchability by disrupting the formation of hydrogen bonds within cellulose chains [46]. Despite these advances, the stretchability of all-cellulose hydrogels remains limited, with a maximum value typically below 250 % [42]. Again, such limitation arises from the presence of rigid AGU rings and abundant random hydrogen bonding networks, which restrict their applicability in areas where high stretchability is needed.

In this study, we introduce a straightforward strategy to produce a highly stretchable all-cellulose-based hydrogel by precisely controlling the molecular architecture of cellulose chains and their associated hydrogen bonding network. The substantial reduction in rigidity of cellulose chains can be achieved through a periodate oxidation ring-opening reaction, which results in the formation of cellulose strands with enhanced chain mobility. The dialdehyde groups formed on the cellulose chains are subsequently converted into primary hydroxyl groups, providing a chemical foundation for the formation of inter-chain hydrogen bonds. The dialcohol nanocellulose tends to aggregate at a high concentration, allowing for its assembly into a hydrogel through the removal of excess water using a vacuum filtration process. The resulting hydrogel exhibits superb stretchability (>40000 %) due to the combination of a relatively linear molecular structure and a well-regulated hydrogen bonding network. Furthermore, this fully physically crosslinked structure imparts the hydrogel with instant and efficient self-healing properties (within seconds). Based on these properties, we showcase the application of this all-cellulose hydrogel as strain sensors and electrodes for detecting human physiological signals, such as human motions and electrocardiography (ECG). We believe that this strategy not only enables a comprehensive exploration of cellulosic materials but also has tremendous potential for developing high-performance hydrogel and other functional materials.

Result and discussion

Fabrication of super-stretchable all-cellulose hydrogel

All-cellulose hydrogels typically exhibit high stiffness with limited stretchability due to the presence of rigid anhydroglucose unit (AGU) ring structures in the backbone, along with the robust interchain hydrogen bonding interactions, as depicted schematically in Scheme 1**a**. Therefore, we hypothesize that by modifying the cellulose structure and regulating their interchain interactions, it is possible to create a highly stretchable all-cellulose hydrogel. Aiming to enhance the chain flexibility, periodate oxidation was employed to open the AGU ring structure by selectively cleaving C2-C3 linkage, converting secondary hydroxyls into aldehyde groups. Additionally, the two aldehyde groups were subsequently reduced to two primary hydroxyl groups. To concentrate the DCNRs and promote their proximity for the formation of a stretchable hydrogel, vacuum filtration was employed to remove excess water (Scheme 1b). After the conversion from the secondary hydroxyl groups (C2 and C3 position) on cellulose rings to primary hydroxyl groups, the rigid AGU ring structures are cleaved into a linear structure which reduces the steric effect of AGU rings. Therefore, this transformation induces the formation of more intermolecular hydrogen bonds and more out-of-plane hydrogen bonds between the obtained dialcohol cellulose nanorods [47]. Thus, when filtration induces a highly concentrated DCNRs suspension, the DCNRs will interact with each other through these abundant hydrogen bonds. Eventually, we successfully developed an ultra-stretchable all-cellulose hydrogel that exhibits an exceptional strain exceeding 40000 %. Furthermore, this hydrogel also demonstrates a rapid self-healing capability.

Characteristics of dialcohol cellulose nanorods (DCNRs)

Throughout the chemical modification of the northern bleached softwood kraft (NBSK) pulp, the products resulting from each individual step were characterized to monitor the progression of the reaction process. As shown in Fig. 1**a**, the original pulp suspension appeared opaque and exhibited severe aggregation, which can be attributed to the large dimensions of the pulp fibers. Following periodate oxidization, the suspension remained opaque; however, it exhibited improved stability, which can be attributed to the reduction in fiber length caused by the oxidation. The high opaqueness of the suspension suggested the presence of severe aggregation, which can be ascribed to the formation of hemiacetal or acetal linkages between the aldehyde groups [48]. Nevertheless, a transparent and stable suspension can be achieved following mechanical blending and borohydride reduction. Optical microscopy was employed to observe the morphological change of the pulp during the oxidation and reduction process. As shown in Fig. S1, the original NBSK pulp exhibited long cellulose microfiber structures. After oxidation, the long pulp fibers were oxidized and converted to short microfibers due to the ring-opening reactions of cellulose and the cleavage of the glycosidic linkage during oxidation. However, due to the formation of hemiacetal/acetal linkages between aldehyde groups, the cellulose fiber cannot separate into nanostructured cellulose. Further reducing the dialdehyde cellulose into DCNRs will reduce all the hemiacetal/acetal linkages and thereby

Please cite this article in press as: Y. Zhang et al., Materials Today (2024), https://doi.org/10.1016/j.mattod.2024.02.007

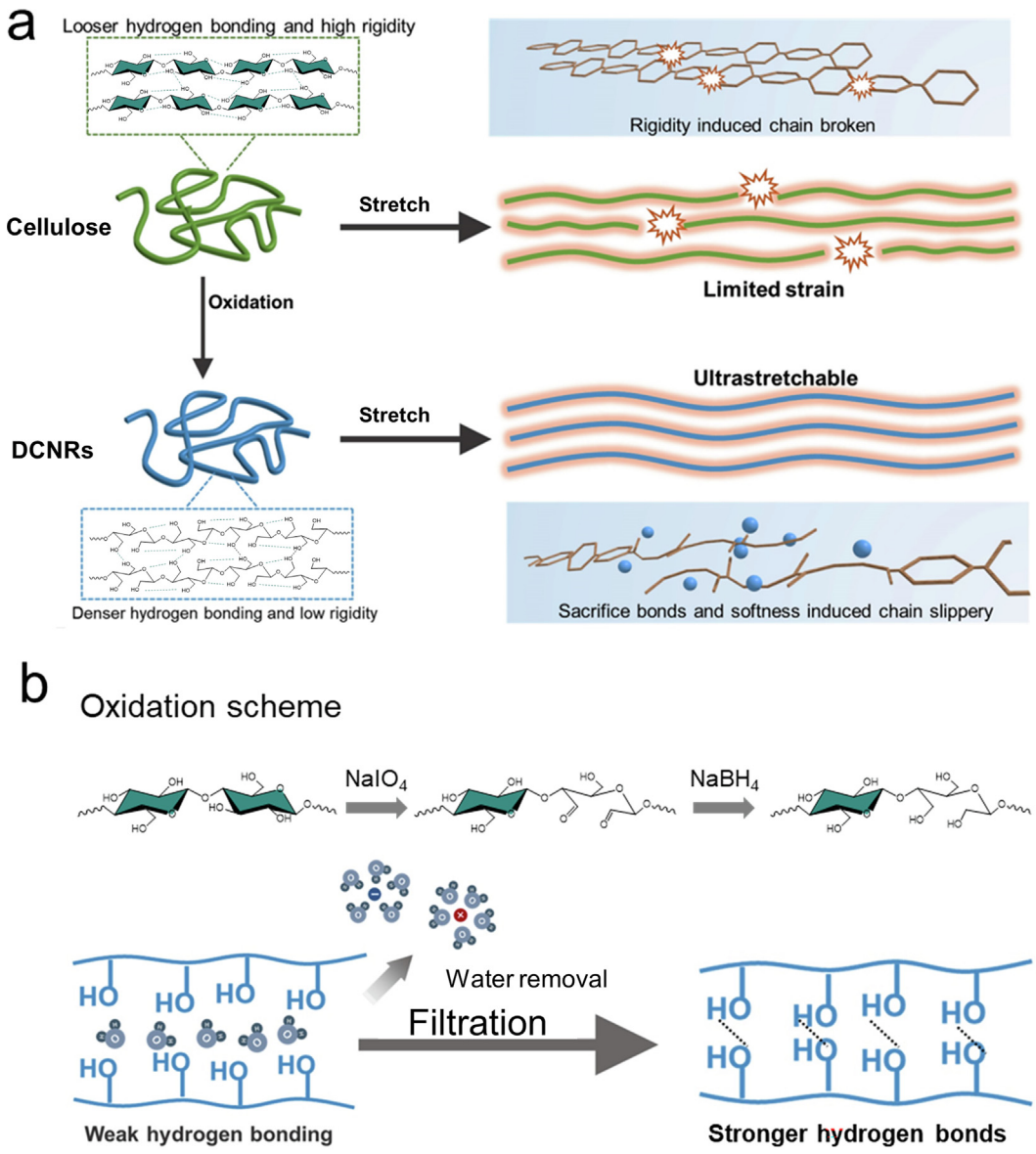

SCHEME 1

Schematic illustration showing that **a)** cleaving the rigid anhydroglucose unit (AGU) rings will increase chain flexibility and promote the re-formation of hydrogen bonds during stretching. **b)** the fabrication process of DCNRs hydrogel.

eliminate the microstructures under optical microscopy, suggesting that the sizes were further reduced and nanostructured cellulose was formed. UV–Vis spectra (Fig. 1b) were further utilized to show the transmittance of dialdehyde cellulose (DACs) and DCNRs suspension. The results clearly indicate a significant increase in the transmittance at 650 nm, rising from 25.8 % for DACs to approximately 95.6 % for DCNRs. Additionally, it is evident that the absorbance peak associated with carbonyl groups at around 250 nm disappears in the DCNRs suspension, further confirming the successful reduction of aldehyde groups. In order to further verify the transformation from cellulose to DCNRs, ATR-FTIR was employed. As shown in Fig. 1c, the ATR-FTIR spectra of NBSK pulp, DACs, and DCNRs all exhibited characteristic cellulose absorption peaks, including O–H stretching vibration at approximately 3330 cm^{-1}, C–H stretching vibration at around 2900 cm^{-1}, $-CH_2$ symmetric bending vibration at 1456 cm^{-1}, C–H bending vibration at 1371 cm^{-1}, C-O-C glycosidic linkage stretching vibration at 1140 cm^{-1}, and C-O stretching vibration at 1053 cm^{-1}[49]. After periodate oxidation, the DACs spectrum exhibited a small peak at 1730 cm^{-1} and an intensified peak at 880 cm^{-1}, which can be assigned to the carbonyl groups and the newly formed hemiacetal linkages between the aldehyde groups and hydroxyl groups, respectively, thus confirming the successful oxidization process. After borohydride reduction, the peaks observed at both 1730 cm^{-1} and 880 cm^{-1} vanished, while the peak at 3330 cm^{-1} became more pronounced, confirming the successful reduction of aldehyde groups to hydroxyl groups. The oxidation degree of DCNRs was calculated to be 70.6 % according to the titration result based on aldehyde content.

The morphology of DCNRs was observed by TEM and AFM. As shown in Fig. 1d, the DCNRs exhibited a typical rod-like structure with an average length of 94.9 ± 1.6 nm and an average

Please cite this article in press as: Y. Zhang et al., Materials Today (2024), https://doi.org/10.1016/j.mattod.2024.02.007

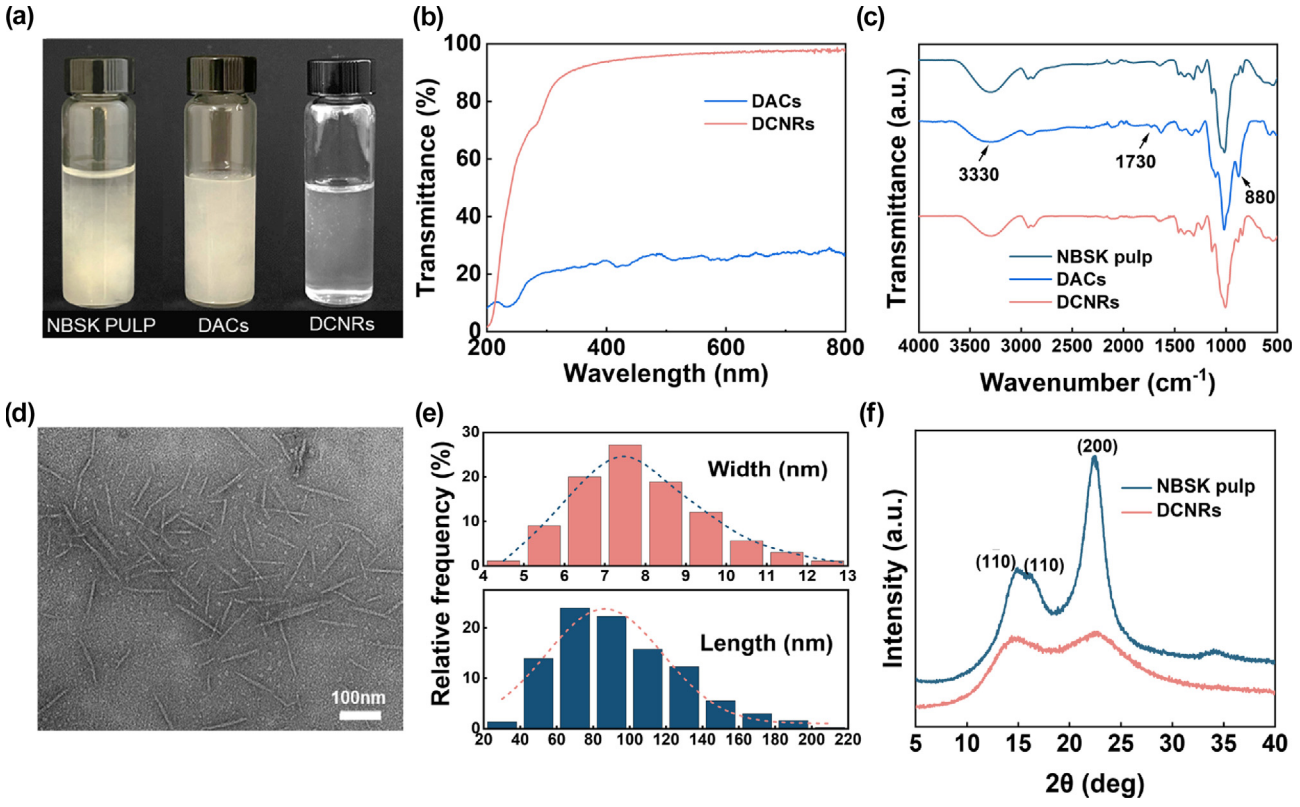

FIG. 1

Characterizations of NBSK pulp, DACs, and DCNRs. **a)** Photos of aqueous NBSK pulp, DACs and DCNRs suspension. **b)** UV–Vis spectra of 0.5 wt% DACs and DCNRs suspensions. **c)** FTIR spectra of NBSK pulp, DACs and DCNRs. **d)** TEM images of DCNRs and **e)** corresponding width and length distributions. **f)** XRD diffractogram of NBSK pulp and DCNRs.

width of 8.0 ± 0.1 nm (Fig. 1e). The AFM image (Fig. S2) also displayed similar rod-like structure consistent with the TEM image. In addition, Fig. 1f shows the X-ray diffraction patterns of NBSK pulp and DCNRs. The NBSK pulp exhibits typical diffraction peaks of Cellulose I at 2θ = 14.7° ($1\bar{1}0$), 16.5° (110) and 22.6° (200) [50]. Interestingly, the XRD diffractogram of DCNRs revealed a noticeable reduction in peak intensity, particularly for the (200) peak at 22.6°. This suggests that the chemical reactions have disrupted the crystalline structure. The considerable decrease in peak intensity observed for the (200) crystal plane suggests that the crystal damage primarily occurs at the axial position of the cellulose chains [51]. In cellulose crystals, the hydroxyl groups are situated at the equatorial position of the AGU ring, contributing to the intra-sheet hydrogen bonding interactions. Meanwhile, inter-sheet stacking is primarily governed by Van der Waals interactions, forming 200 crystal plane. After the conversion of the secondary hydroxyl groups into primary hydroxyls through ring-opening interactions, the resulting hydroxyl groups exhibit a higher degree of freedom, enabling them to rotate away from the equatorial position. Such rotation ultimately leads to the disruption of the crystal plane, particularly affecting the (200) plane held together by Van der Waals interactions. Based on the Segal empirical equation, the crystallinity index dropped from 70.9 % to 26.7 %.

Characteristics of the DCNR hydrogel

The all-cellulose hydrogel was prepared through a simple vacuum filtration of 0.6 wt% DCNR suspension. During filtration, the DCNRs tend to accumulate on the 0.45 μm nylon filter, leading to the formation of a gel-like material. This is to our surprise since the measured particle sizes of the DCNRs from both AFM and TEM are close to 100 nm in length and a few nm in width. Therefore, it is not expected that the DCNRs can be retrained by the filtreation membrane with 0.45 μm pore size. It should be noted that no gel-like material can be obtained when filtering diluted 0.05 wt% DCNRs suspension, suggesting that the DCNRs tend to aggregate at high concentration, further confirming the strong hydrogen bonding formed among the DCNRs. To further verify the impact of concentration on the particle size of the DCNRs, dynamic light scattering (DLS) was employed to evaluate the hydrodynamic diameter of the DCNRs suspension at varied concentrations. As shown in Fig. S3, the 0.05 wt% DCNRs showed two peaks centered at 8.7 nm and 78.8 nm. Notably, both peaks significantly shifted to larger values of 43.8 nm and 295.3 nm at 0.6 wt% concentration, and then to 122.4 nm and 712.4 nm at a concentration of 3 wt%, clearly indicating particle aggregation at increased concentration. Therefore, when filtering the DCNRs suspension at 0.6 wt%, the DCNRs aggregates can be retained on the filtration membrane as the concentration increases, resulting in a gel-like material.

Further characterization of the prepared all-cellulose hydrogel revealed its characteristic non-Newtonian behavior, showing a liquid-like behavior under a low shear rate and solid-like behavior under a high shear rate. This phenomenon is presented in Fig. 2**a**&b. Under static condition, the all-cellulose hydrogel flows slowly over time due to gravity, displaying a liquid-like

Please cite this article in press as: Y. Zhang et al., Materials Today (2024), https://doi.org/10.1016/j.mattod.2024.02.007

behavior (Fig. 2a). However, when a hydrogel ball is dropped from a height, it demonstrates elastic and solid material characteristics by bouncing back (Fig. 2b). Rheology tests were employed to further characterize the non-Newtonian behavior of the all-cellulose hydrogel. As shown in Fig. 2c, at low frequency, the loss modulus G'' surpassed the storage modulus G', indicating a liquid-like structure. However, with increasing frequency, the G' and G'' intersected, and in the high frequency range, the G' exceeded G'', signifying a solid-like behavior. The rheological test further confirmed the recovery ability, as depicted in Fig. 2d. Initially, as the strain increased, the storage modulus G' remained stable, but under high strain, it started to decrease due to the disruption of the hydrogel network. However, as the strain gradually returned to a lower range, the G' also recovered correspondingly, indicating the self-recovery ability. This observation confirms the non-Newtonian nature of the hydrogel and is consistent with the findings presented in Fig. 2a&b.

Mechanical properties of DCNRs hydrogels were investigated by tensile tests. As shown in Fig. 2e, the DCNRs contents greatly influenced the mechanical properties of the all-cellulose hydrogel. With the increase of DCNRs content from 23.3 % to 28.8 %, the tensile stress increased gradually from 7 kPa to 25 kPa and the tensile modulus also increased accordingly from 1.7 kPa to 9 kPa (Fig. 2f). For the tensile strain, when the DCNRs contents were 23.3 % to 28.8 %, the tensile strain all exceeded 10000 % (detection range of our Instron 5969, Fig. S4). When the DCNRs content was increased to 50.0 %, the tensile strain decreased to 242 %, which was due to the decreased water content restricting the movement of DCNRs chains. However, the hydrogel showed much higher stress (281 kPa) and modulus (189 kPa) compared to those with low DCNRs content. In addition, the all-cellulose hydrogel also showcased remarkable self-healing capabilities attributed to its fully-physically crosslinked structure. As shown in Fig. 2g, a piece of hydrogel was cut into two parts, with one piece dyed blue for enhanced visibility. After being recombined for 2 mins, the two pieces seamlessly healed together, resulting in a fully restored hydrogel. The self-healing behavior of the all-cellulose hydrogel under different healing periods was evaluated through the stress–strain curves. As shown in Fig. S5a, under different healing periods (10, 30, and 60 s), the healed hydrogel displayed similar stress–strain curves with a tensile strength of ~ 7 kPa. The strains of all the healed samples exceeded 10000 %, which was the upper limit of the Instron machine. According to the tensile stress, we can calculate the self-healing efficiency by tensile stress after healing/original tensile stress, and the self-healing efficiency of the all-cellulose hydrogel under different healing periods was ~ 100 %. Optical microscopy was employed to observe the incision of the all-cellulose hydrogel during the healing process. As shown in Fig. S5b, the as-cut hydrogel exhibited an obvious incision. After healing for 30 s, the incision was gradually merged; while after healing for 60 s, the incision between two pieces of all-cellulose hydrogel nearly disappeared. Due to the conversion from secondary hydroxyl groups to primary hydroxyl groups by the ring-opening oxidation and reduction, the intermolecular hydrogen bonds and out-of-plane hydrogen bonds between DCNRs were greatly enhanced [47]. Therefore, during the cutting

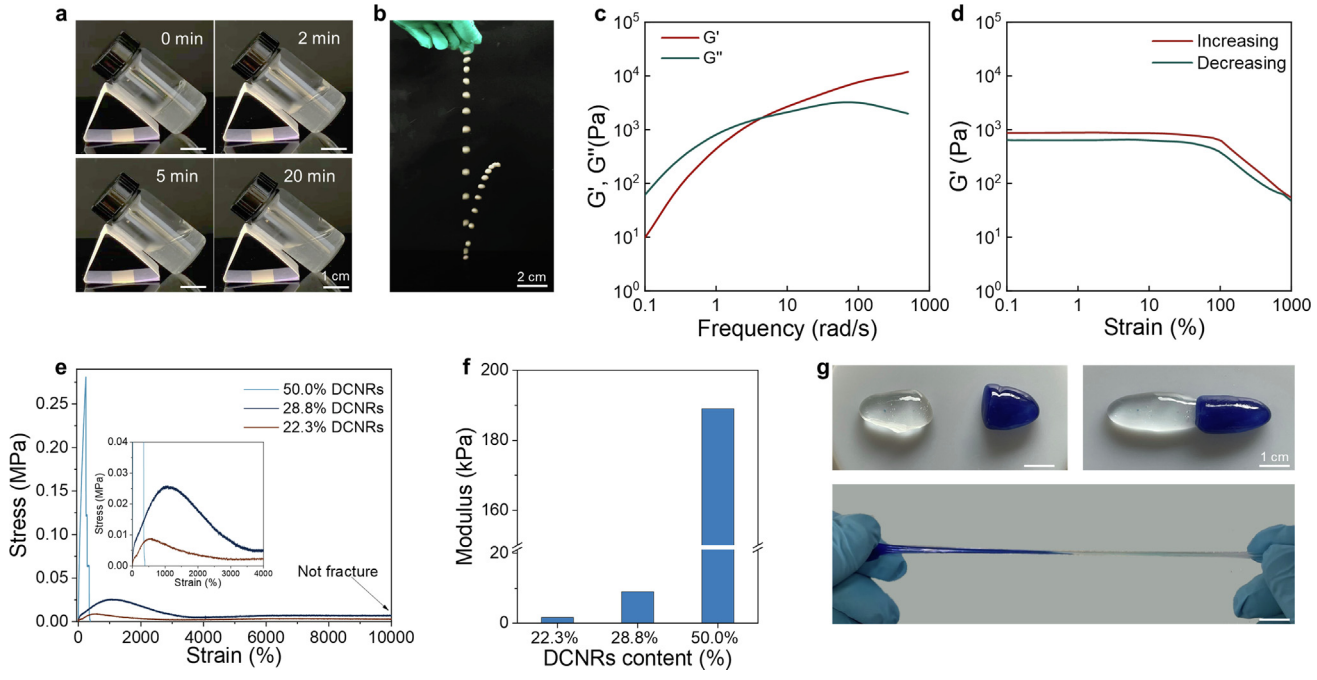

FIG. 2

Characteristics of DCNRs hydrogel. a) Photos showing the fluid behavior of DCNRs hydrogel under static conditions (Scale bar: 1 cm). b) Snapshots showing the DCNRs hydrogel ball bouncing back after being dropped from a height of 0.5 m above the ground (Scale bar: 2 cm). c) Frequency sweep of DCNRs hydrogel. d) The storage modulus G' of the DCNRs hydrogel during the strain amplitude sweep (from 0.1 % to 1000 % and back to 0.1 %). e) Stress–strain curves under different DCNRs contents, and (f) the corresponding modulus. g) Photos of the self-healing process of the DCNRs hydrogel (with one piece being stained with methylene blue, Scale bar: 1 cm).

Please cite this article in press as: Y. Zhang et al., Materials Today (2024), https://doi.org/10.1016/j.mattod.2024.02.007

and healing process of the all-cellulose hydrogel, the hydrogen bonds between dialcohol cellulose nanorods can be quickly dissociated and reformed, inducing nearly instantaneous self-healing behavior. Additionally, Fig. S6 also showed that the hydrogel was capable of recovering from various strains. Furthermore, the all-cellulose hydrogel exhibited outstanding printability, allowing it to be easily injected through a syringe (Fig. S7a) and utilized as ink for writing letters (Fig. S7b). This quality makes it a promising candidate for advanced applications as an injectable ink.

High stretchability of the DCNR hydrogel

In addition to the self-healing property and printability, the all-cellulose hydrogel exhibited record-high and unprecedented stretchability exceeding 40000 % strain (Fig. S8). As shown in Fig. 3**a**, a piece of hydrogel (1 cm) can be stretched to 4.42 m, corresponding to a strain of 44200 %, surpassing all the reported all-cellulose hydrogels (Table S1). After drying at 80 °C for an hour, a flexible and smooth fiber with a width of ~ 47 μm can be obtained. SEM was utilized to observe the morphology of the hydrogel derived fibers. As displayed in Fig. 3b&c, the hydrogel derived fiber exhibited exceptional flexibility, allowing it to withstand twisting and be easily tied into various knotted structures. This manifests that the ultrastretchable all-cellulose hydrogel has the potential to fabricate flexible cellulose fibers through a straightforward process of stretching and drying.

The remarkable ultrastretchability of the all-cellulose DCNR hydrogel can be attributed to its unique physically crosslinked network structure, as well as its non-Newtonian behavior. During the gradual stretching process, the hydrogel exhibited a characteristic viscous behavior, as depicted in Fig. 2c. The viscous behavior enables the DCNRs to be drawn out. The abundant primary hydroxyl groups facilitate the formation of dynamic hydrogen bonds among the DCNRs during the stretching process, resulting in an exceptional level of stretchability that surpasses previous records. The fiber showed vivid birefringence under polarized optical microscopy (POM) (Fig. 3d), indicating that the DCNRs exhibited orientation during the stretching process. The DCNR fiber also demonstrated high mechanical strength, showing a high tensile stress reaching up to 226 ± 34 MPa and a strain of 3.5 %, with a high Young's modulus of 9.4 ± 1.1 GPa (Fig. 3e). As shown in Fig. 3f, a dried DCNR fiber with the diameter of 87 μm can lift a weight of 100 g, showing its high mechanical performance.

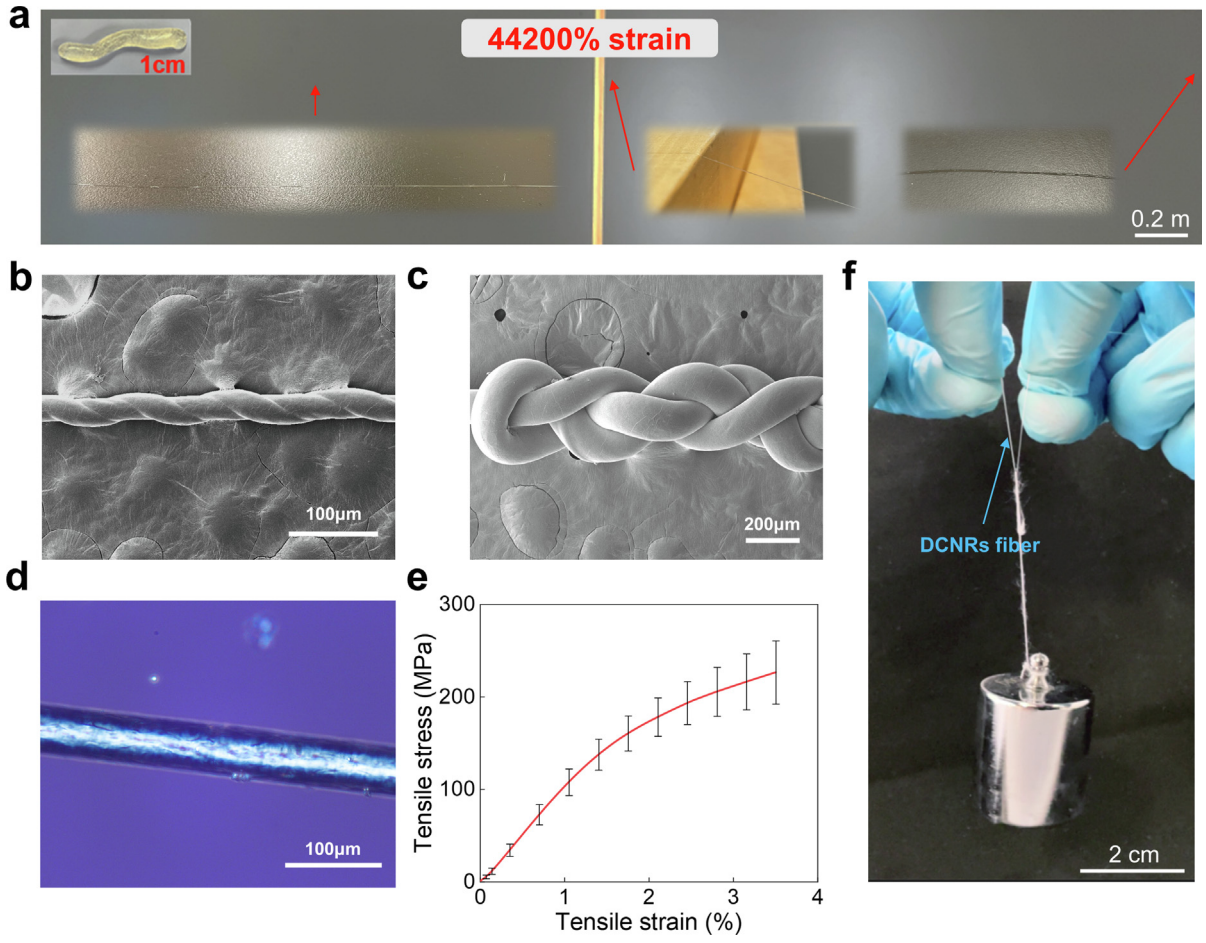

FIG. 3

Characterization of stretchability of DCNRs hydrogel and dried fiber. **a)** Photos of DCNRs hydrogel before and after stretching. SEM images of dried DCNRs fiber **b)** after twisting and **c)** with knots. **d)** Polarized optical microscopy (POM) image of the dried DCNRs fiber. **e)** Average stress–strain curve of dried DCNRs fiber **f)** Photos of DCNRs fiber holding a 100 g weight.

Please cite this article in press as: Y. Zhang et al., Materials Today (2024), https://doi.org/10.1016/j.mattod.2024.02.007

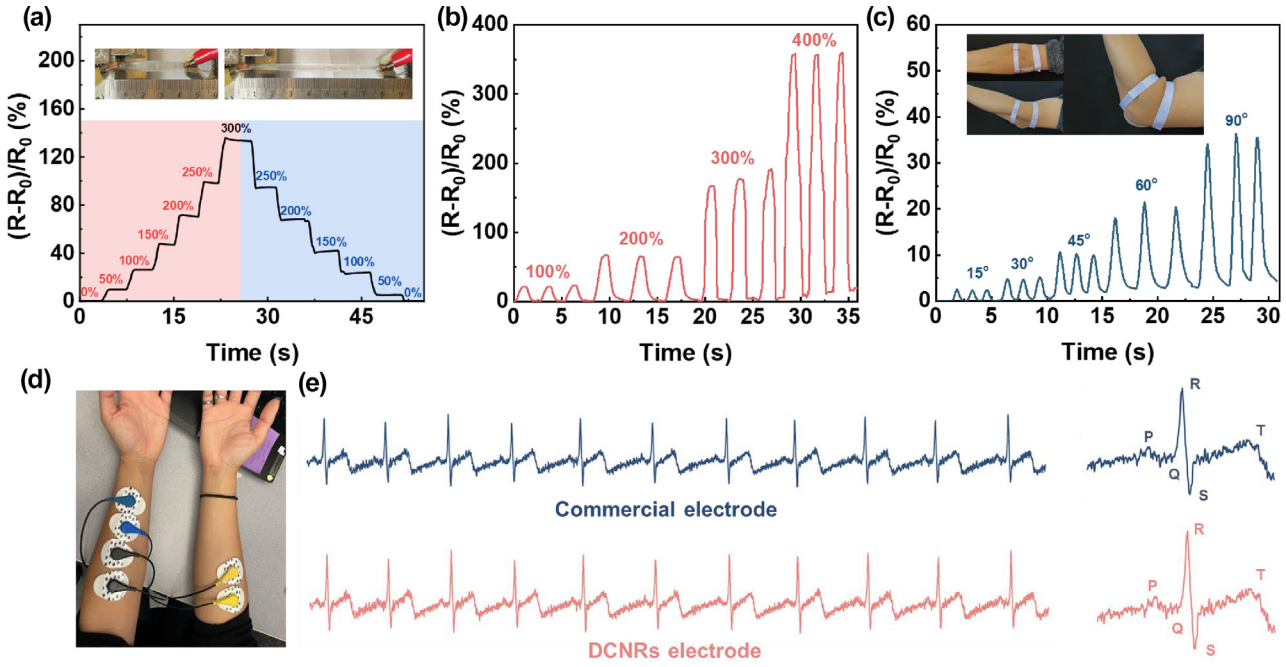

FIG. 4

Applications of DCNRs hydrogel-based sensors. **a)** The relative resistance changes of the sensor during the stretching and releasing process under strains from 0% to 300%. **b)** Relative resistance changes of the sensor under different tensile strains (3 cycles for each strain). **c)** Relative resistance change of hydrogel sensor for monitoring elbow bending of a volunteer. **d)** Photograph of attachment of commercial and DCNRs hydrogel-based electrodes. **e)** Spectrum of ECG signal obtained from commercial electrodes and DCNRs electrodes.

Application as sensors and electrodes

For the preparation of the all-cellulose hydrogel, the DCNR suspension after borohydride reduction was employed as-is, without eliminating the residual salts from sodium borohydride ($NaBH_4$) and monobasic sodium phosphate (NaH_2PO_4). After reduction, it is expected that the suspension encompassed the subsequent ions: Na^+, $H_2PO_4^{2-}$, and $B(OH)_4^-$, which can offer ionic conductivity to the hydrogel (0.025 S/cm, Fig. S9). Given the ultrastretchability, flexibility as well as the existence of free ions, we speculated that the all-cellulose hydrogel could serve as an ion-conductive motion sensor and apply as electrocardiogram (ECG) electrodes for monitoring physiological signals. Firstly, the sensing performance under different strain ratios was presented in Fig. 4**a**. With the increased external strain from 0 % to 300 %, the relative resistance change ($\Delta R/R_0$) of the hydrogel gradually increased from 0 to 136 %. After stepwise releasing the external strain, the $\Delta R/R_0$ could recover to the corresponding value, suggesting a low hysteresis and high reliability of transducing strain signals. Besides, cyclic stability under different strains was also evaluated from 100 % to 400 % strain as shown in Fig. 4b. Under the same strain, the output resistance signals were highly stable and repeatable, indicating a high stability of the hydrogel sensor. Therefore, the all-cellulose hydrogel was employed as a wearable sensor to monitor human movements in real time. As shown in Fig. 4c&Movie S1, when the sensor was mounted on the volunteer's elbow and finger, the relative resistance change was increased when the volunteer performed bending and the bending angle could be reflected by the peak intensity, signifying the potential for the all-cellulose hydrogel in wearable sensors.

In addition to the strain sensitivity, the free ions in the hydrogel also enabled the all-cellulose hydrogel to transduce signals as an ECG electrode. By utilizing ultrastretchability, the hydrogel can be easily coated on the skin (Fig. S10). As shown in Fig. 4d, all-cellulose electrodes, and commercial gel electrodes were fixed on forearms simultaneously to acquire the ECG signals in real-time. Fig. 4e showed the ECG signals obtained through commercial electrodes and all-cellulose hydrogel electrodes. It was obvious that all PQST typical waves were clearly observed for both commercial and our hydrogel electrodes. Besides, by comparing the ECG signals from commercial gel electrodes and all-cellulose hydrogel electrodes, the similarity could reach 99.9 %, indicating the potential of all-cellulose hydrogel for replacing the commercial counterparts. All these results suggest that our all-cellulose hydrogel has great potential for use as wearable sensors and for monitoring physiological signals. These findings highlight the high potential of the ultrastretchable all-cellulose hydrogel for wearable devices.

Conclusion

To sum up, an ultrastretchable all-cellulose hydrogel was fabricated for the first time. Sequential periodate oxidation and borohydride reduction can lead to the breakage of rigid AGU ring structure, as well as the conversion of two secondary hydroxyl groups on each AGU ring to primary hydroxyl groups. An ultrastretchable all-cellulose hydrogel can be facilely formed by vacuum filtration of the dialcohol cellulose nanorods at high concentration, showing fast self-healing properties and unique non-Newtonian behavior. Benefiting from the dynamic hydrogen bonding induced by the primary hydroxyl groups and

Please cite this article in press as: Y. Zhang et al., Materials Today (2024), https://doi.org/10.1016/j.mattod.2024.02.007

opened ring structure, the hydrogel can rapidly self-heal after breaking and can be stretched to over 40000 % strain without breaking. In addition, the DCNRs hydrogel can be stretched into a dried cellulose fiber with excellent flexibility and high mechanical strength. Furthermore, the hydrogel can serve as an ionic-conductive motion sensor and ECG electrode due to its inherent free ions, showing excellent reproducibility as compared to commercial ECG gel electrodes. This innovative approach offers a streamlined method for crafting ultrastretchable all-cellulose hydrogels, holding significant promise for advanced sensor and health monitoring applications.

Methods

Materials: Sodium *meta*-periodate ($NaIO_4$, >99.8 %), sodium chloride (NaCl, >99 %), sodium borohydride ($NaBH_4$, 99 %), monobasic sodium phosphate (NaH_2PO_4, 99 %) were obtained from Thermo fisher scientific. Northern bleached softwood kraft (NBSK) pulp was provided by the Pulp and Paper Centre at UBC (Vancouver, Canada). All the reagents were used as received without further purification.

Synthesis of dialdehyde cellulose (DAC): The DAC was prepared by adding 1 g of NBSK in 100 mL deionized water and then stirred for at least 12 h at room temperature, followed by adding $NaIO_4$ (1.32 g) and NaCl (3.87 g) to the cellulose suspension and stirring with a magnetic stirrer for 72 h. To protect the periodate from decomposition, the mixture was covered with aluminum foil during the oxidation process. The mixture was then dialyzed against deionized water for one week to remove residual chemicals.

Synthesis of dialcohol cellulose nanorods (DCNRs) and hydrogel: The DCNRs were synthesized by reducing the DAC using sodium borohydride. Before borohydride reduction, the DAC suspension was blended by high-speed mechanical blending (Vitamix 5200) for 15 min to ensure complete dispersion. Then, 0.5 g $NaBH_4$ (per gram of cellulose) and 0.025 mol/L of NaH_2PO_4 were added to the DAC suspension and the reaction was allowed to proceed for 12 h at room temperature under magnetic stirring, yielding DCNRs of approximately 0.6 wt% concentration. The residual salts from the buffer and reducing agent were kept in the suspension, and the suspension was vacuum filtrated through a 0.45 μm nylon filter paper for 70 h at room temperature, leading to the formation of ultrastretchable all-cellulose hydrogel.

Measurements and Characterizations: Cary 60 UV – vis spectrophotometer (Agilent Technologies, Santa Clara, CA, USA) was utilized to measure the transmittance and absorbance of 0.5 wt% DCNRs suspension at a wavelength of 220 to 800 nm with a scanning rate of 100 nm min^{-1}. TEM images were acquired using a Hitachi H7600 transmission electron microscope operating at an acceleration voltage of 80 kV. For sample preparation, drops of a 0.01 wt% DCNRs suspension were carefully deposited onto a glow-discharged TEM grid coated with a carbon layer. Excess liquid was removed by gently blotting with filter paper. Subsequently, the samples were dried at room temperature. To enhance contrast, a drop of a 2 % uranyl acetate solution was applied to negatively stain the DCNRs. Widths and lengths of DCNRs were measured from TEM images using Nano Measurer 1.2 software of more than 200 individual nanorods.

The mechanical properties were measured by an Instron machine (Instron 5969) with a crosshead speed of 100 mm/min and a load cell of 500 N in a conditioning room with 55 % relative humidity at 25°C For better recording of the signals, the hydrogel was fixed between two glass slides. The morphologies of fibers and the self-healing process were observed by an optical microscope (Polyvar, OPTI-TECH, Canada). The fibers/hydrogels were coated on a glass slide.

The aldehyde content was determined by titration. Firstly, ~100 mL of dialdehyde cellulose suspension (0.1 wt%) was adjusted to pH = 3 by adding 0.1 mol/L HCl. Then, hydroxylamine hydrochloride was added to the suspension and reacted for 2 h. The suspension was titrated using 0.1 mol/L NaOH to pH = 3. The aldehyde content was calculated as: $\frac{c(\mathrm{NaOH})\times v(\mathrm{NaOH})}{m(\mathrm{DAC})}$, where c(NaOH) is the concentration of NaOH and v(NaOH) is the volume of NaOH consumed, and m(DAC) is the weight of DAC in the suspension. The oxidation degree was calculated as: $\frac{\text{aldehyde content}}{\text{mole of AGU rings per g of DAC}} \times \frac{1}{2} \times 100\%$.

The morphology of the DCNRs was characterized using an atomic force microscope (MultiMode8, Bruker USA Inc.). A drop of 0.001 wt% DCNR suspension was deposited onto a freshly peeled mica surface and allowed to dry at ambient conditions before measurement. The experiments were conducted in peak force tapping mode using aluminum-coated antimony-doped silicon cantilevers with a spring constant of 40 N/m and a resonant frequency of 300 kHz. The 2D height images were processed using Nanoscope Analysis software.

FTIR spectra of the samples were collected using an INVENIO-S attenuated total reflectance Fourier transform infrared spectroscopy (ATR-FTIR, Bruker Optics Pty. Ltd., Billerica, MA, USA) with single bounce diamond crystal. All the spectra of measured samples were collected from 400 to 4000 cm^{-1}, comprising a total of 16 scans, with a resolution of 4 cm^{-1}.

The size distribution of each sample was analyzed using dynamic light scattering (DLS). The Malvern Zetasizer Nano ZS was utilized for all measurements, with data collection based on monitoring the intensity of scattered light at a 90° scattering detector angle and a temperature of 21 °C.

X-ray diffraction (XRD) experiments were conducted using a D8 Advance Bragg-Brentano Diffractometer (Bruker, Billerica, MA, USA) equipped with a long fine-focus Co X-ray tube operating at 35 kV and 40 mA. The XRD diffractogram of NBSK pulp and freeze-dried DCNRs were recorded over a 2θ range of 5° to 65°, with a scan rate of 1° min^{-1}. Subsequently, the obtained 2θ values were shifted to correspond to a Cu target using Jade software. The crystallinity index (CrI) was determined by applying the Segal empirical equation.

The viscoelastic rheological properties of the hydrogel were assessed using a TA Instruments AR 200 rotational rheometer at room temperature (25 °C). A parallel plate with a 25 mm diameter and a gap distance of 1 mm was utilized to generate a uniform shear rate. The sample was subjected to torsional flow in both CR and CS modes to determine its viscous behavior and yield stress (τy). In addition, oscillatory tests were carried out to evaluate the viscoelastic behavior of the sample. The sample was allowed to

Please cite this article in press as: Y. Zhang et al., Materials Today (2024), https://doi.org/10.1016/j.mattod.2024.02.007

reach equilibrium temperature with the measuring system for at least 10 min.

The mechanical properties of derived DCNRs fibers were evaluated using TA instrument Q800 dynamic mechanical analyzer (DMA, New Castle, USA) with an 18 N load cell. The tests were conducted at room temperature, and a range of loads from 0.01 N to 1.8 N was applied to the fibers. To prevent any premature failure before testing, The fibers with diameters ranging from 50 μm to 110 μm were loaded into clamps with a paper frame and a preload force of 0.01 N.

The strain sensor was constructed by placing the hydrogel between two 3 M VHB adhesive tapes. The VHB tapes were used to adhere the sensor to the skin and prevent solvent evaporation. The resistance of the hydrogel was measured in real-time using a digital source meter (Keithley 2450, USA). The relative change in resistance was calculated using the formula $(R - R_0)/R_0 * 100\ \%$, where R represents the resistance under different strains, and R_0 represents the resistance at the initial state without any strain.

The performance of the fabricated electrodes was evaluated by monitoring ECG signals using the DCNRS hydrogel to replace the commercial gel of T3425 UniGel electrodes and comparing it to the ECG signals obtained from commercial T3425 UniGel electrodes using the T9306M EKG sensor package (Thought Technology, Canada). BioGraph Infiniti (Thought Technology, Canada) was utilized to visualize and display the ECG signals obtained. All signal measurements were performed at room temperature. Six electrodes were placed on the left and right forearms of the test subject and simultaneously connected to the T9306M EKG sensor to acquire accurate data. All tests involving human volunteers were carried out in full compliance with all local laws and institutional ethical guidelines. Full and informed consent was given by each subject for these experiments. ECG tests were performed under approval (UBC CREB H21-03312 by UBC Clinical Research Ethics Board (CREB)).

CRediT authorship contribution statement

Yifan Zhang: Writing – review & editing, Writing – original draft, Methodology, Investigation, Conceptualization. **Xia Sun:** Writing – original draft, Methodology, Investigation. **Yuhang Ye:** Investigation. **Hale Oguzlu:** Investigation. **Yeling Zhu:** Investigation. **Jiaying Zhu:** Investigation. **Katherine Le:** Investigation. **Pu Yang:** Investigation. **Feng Jiang:** Writing – review & editing, Supervision, Resources, Funding acquisition, Conceptualization.

Data availability

Data will be made available on request.

Declaration of competing interest

The authors declare that they have no known competing financial interests or personal relationships that could have appeared to influence the work reported in this paper.

Acknowledgements

This research was undertaken, in part, thanks to funding from the Canada Research Chairs program (231928), the Natural Sciences and Engineering Research Council of Canada (NSERC, RGPIN-2018-06818), and Canada Foundation for Innovation—John R. Evans Leaders Fund (CFI-JELF #37517). We also acknowledge Profs. Scott Renneckar, Emily Cranston, Orlando Rojas, UBC Pulp and Paper Centre, and UBC Bioimaging Facility for accessing their instruments used in this project. The authors thank Harishkumar Narayana from UBC for help on ECG experiments.

Appendix A. Supplementary data

Supplementary data to this article can be found online at https://doi.org/10.1016/j.mattod.2024.02.007.

References

[1] C.F. Guimaraes et al., Adv. Mater. 33 (2021), https://doi.org/10.1002/adma.202006582 e2006582.
[2] Y. Li et al., Adv. Funct. Mater. 23 (2013) 660–672, https://doi.org/10.1002/adfm.201201708.
[3] D. Zhao et al., Adv. Mater. 33 (2021), https://doi.org/10.1002/adma.202000619 e2000619.
[4] L. Hu et al., Adv. Mater. 35 (2023), https://doi.org/10.1002/adma.202205326 e2205326.
[5] W. Li et al., Adv. Funct. Mater. 33 (2023), https://doi.org/10.1002/adfm.202213485.
[6] Y. Ye et al., Chem. Rev. 123 (2023) 9204–9264, https://doi.org/10.1021/acs.chemrev.2c00618.
[7] Z. Wang et al., Adv. Funct. Mater. 28 (2018), https://doi.org/10.1002/adfm.201804560.
[8] Z. Zhang et al., Chem. Eng. J. 433 (2022), https://doi.org/10.1016/j.cej.2021.134488.
[9] L. Li et al., Nat. Commun. 11 (2020) 62, https://doi.org/10.1038/s41467-019-13959-9.
[10] D. Liu et al., Small 18 (2022) e2203258.
[11] D. Zhao et al., Carbohydr. Polym. 256 (2021), https://doi.org/10.1016/j.carbpol.2020.117580 117580.
[12] X. Luo et al., Adv. Funct. Mater. 31 (2021), https://doi.org/10.1002/adfm.202104928.
[13] H. Fang et al., Chem. Eng. J 365 (2019) 153–164, https://doi.org/10.1016/j.cej.2019.02.030.
[14] J. Chong et al., Nat. Commun. 14 (2023) 2206, https://doi.org/10.1038/s41467-023-37948-1.
[15] H. Liu et al., Nat. Commun. 13 (2022) 3420, https://doi.org/10.1038/s41467-022-31051-7.
[16] A. Priya et al., J. Chem. Technol. Biotechnol. 97 (2021) 381–390, https://doi.org/10.1002/jctb.6675.
[17] S.A. Mason et al., Front. Chem. 6 (2018) 407, https://doi.org/10.3389/fchem.2018.00407.
[18] R. Geyer, Production, use, and fate of synthetic polymers, in: T.M. Letcher (Ed.), Plastic Waste and Recycling, Academic Press, Cambridge, 2020, pp. 13–32.
[19] H. Miyajima et al., Biomater. 32 (2011) 6754–6763, https://doi.org/10.1016/j.biomaterials.2011.05.072.
[20] R. Ajdary et al., Adv. Mater. 33 (2021) e2001085.
[21] J. Wu et al., Acta Biomater. 88 (2019) 102–110, https://doi.org/10.1016/j.actbio.2019.01.067.
[22] X. Wang et al., Soft Matter 7 (2011) 211–219, https://doi.org/10.1039/c0sm00632g.
[23] M.F. Moradali, B.H.A. Rehm, Nat. Rev. Microbiol. 18 (2020) 195–210, https://doi.org/10.1038/s41579-019-0313-3.
[24] W. Kong et al., Chem. Mater. 31 (2019) 9288–9294, https://doi.org/10.1021/acs.chemmater.9b02463.
[25] X. Shen et al., Green Chem. 18 (2016) 53–75, https://doi.org/10.1039/c5gc02396c.
[26] N. Hu et al., Carbohydr. Polym. 243 (2020), https://doi.org/10.1016/j.carbpol.2020.116480 116480.
[27] Y. Ye et al., Adv. Funct. Mater. 30 (2020), https://doi.org/10.1002/adfm.202003430.
[28] Y. Ye, F. Jiang, Nano Energy 99 (2022), https://doi.org/10.1016/j.nanoen.2022.107374.

[29] Y. Ye et al., Mater. Horiz. 10 (2023) 2667–2676, https://doi.org/10.1039/d3mh00234a.
[30] G. Jiang et al., Res. 2022 (2022) 9814767. https://doi.org/10.34133/2022/9814767.
[31] Y. Zhu et al., Nat. Synth. 2 (2023) 864–872, https://doi.org/10.1038/s44160-023-00315-5.
[32] J. Huang et al., The Innov. Mater. 1 (2023). https://doi.org/10.59717/j.xinn-mater.2023.100029.
[33] P. Zhu et al., Adv. Mater. (2023), https://doi.org/10.1002/adma.202306653 e2306653.
[34] S. Wang et al., Nat. Commun. 13 (2022) 3408, https://doi.org/10.1038/s41467-022-30224-8.
[35] K. Zhang et al., Carbohydr. Polym. 293 (2022), https://doi.org/10.1016/j.carbpol.2022.119673 119673.
[36] Y. Qin et al., Adv. Funct. Mater. 32 (2022), https://doi.org/10.1002/adfm.202201846.
[37] X. Sun et al., Adv. Sens. Res. 2 (2023), https://doi.org/10.1002/adsr.202200045.
[38] Y. Ye et al., Adv. Funct. Mater. 33 (2022), https://doi.org/10.1002/adfm.202209787.
[39] X. Sun et al., Adv. Funct. Mater. 32 (2022), https://doi.org/10.1002/adfm.202202533.
[40] R. Nasseri et al., Nat. Commun. 14 (2023) 6108, https://doi.org/10.1038/s41467-023-41874-7.
[41] R. Tong et al., Biomacromolecules 20 (2019) 2096–2104, https://doi.org/10.1021/acs.biomac.9b00322.
[42] L. Shu et al., Int. J. Biol. Macromol. 230 (2023), https://doi.org/10.1016/j.ijbiomac.2023.123425 123425.
[43] Y. Wang et al., ACS Appl. Mater. Interfaces 11 (2019) 41710–41716, https://doi.org/10.1021/acsami.9b15849.
[44] Y. Hu et al., Carbohydr. Polym. 265 (2021), https://doi.org/10.1016/j.carbpol.2021.118078 118078.
[45] C. Chang, L. Zhang, Carbohydr. Polym. 84 (2011) 40–53, https://doi.org/10.1016/j.carbpol.2010.12.023.
[46] M. Wohlert et al., Cellulose 29 (2021) 1–23, https://doi.org/10.1007/s10570-021-04325-4.
[47] X. Sun et al., The Innovation Materials 1 (3) (2023). https://doi.org/10.59717/j.xinn-mater.2023.100040 100040-1-100040-8.
[48] N. Guigo et al., Cellulose 21 (2014) 4119–4133, https://doi.org/10.1007/s10570-014-0459-0.
[49] F. Jiang, Y.-L. Hsieh, ACS Sustain. Chem. Eng. 4 (2016) 1041–1049, https://doi.org/10.1021/acssuschemeng.5b01123.
[50] F. Jiang, Y.L. Hsieh, Carbohydr. Polym. 95 (2013) 32–40, https://doi.org/10.1016/j.carbpol.2013.02.022.
[51] B. Pingrey, Y.L. Hsieh, Biomacromolecules 23 (2022) 1269–1277, https://doi.org/10.1021/acs.biomac.1c01505.

Please cite this article in press as: Y. Zhang et al., Materials Today (2024), https://doi.org/10.1016/j.mattod.2024.02.007